Electronic Interface Design Considerations for Biomagnetic Sensing Using TMR Sensors

Huxi Wang[1,2], Meraj Ahmad[1,2], Asfand Tanwear[1,2], Negin Ghahremani Arekhloo[1,2], Siming Zuo[1,2], Kianoush Nazarpour[1,3], Hadi Heidari[1,2]

[1] Neuranics Limited, Glasgow, G2 4HF, UK
[2]Microelectronics Lab, James Watt School of Engineering, University of Glasgow, G12 8QQ, UK
[3]School of Informatics, The University of Edinburgh, EH8 9AB, UK

We present a comprehensive design methodology for the electronic interface of a tunneling magnetoresistance (TMR) sensor, which plays a crucial role in determining the detectivity of biomagnetic measurement systems. A theoretical noise model is developed that links sensor detectivity to key design parameters such as the Wheatstone bridge configuration, sensor biasing, and analogue front-end (AFE) noise performance. The model is based on detailed characterization of the TMR sensor and accurately predicts the influence of bias voltage and resistance mismatches on the power supply rejection ratio (PSRR). It shows that the full Wheatstone bridge configuration achieves superior detectivity, and that the PSRR can degrade from near-infinite values to approximately 28 dB under a background magnetic field of 5 µT. Guided by this model, the sensor system is optimized in terms of bridge configuration, bias conditions, and AFE design. Experimental validation confirms a detectivity of 7.4 pT/ √ Hz at 1 Hz and an integrated RMS noise of 20 pT within the 5 to 100 Hz band, under both near-zero and 5 µT magnetic fields. These results surpass those of previously reported TMR-based sensor systems operating in similar frequency bands and under comparable working conditions. The findings highlight the importance of a systematic and integrated approach to electronic interface design for TMR sensors, which supports the development of biomagnetic sensing systems capable of operating without extensive magnetic shielding.

***Index Terms*— Tunnelling magnetoresistance, Magnetic tunnel junction, Wheatstone bridge, sensor interface, analogue front-end, noise, biomagnetic signals.**

I. INTRODUCTION

Tunnelling magnetoresistance (TMR) sensors have emerged as a promising technology in magnetic field sensing due to their exceptional sensitivity, wide dynamic range, low power consumption and compact form factor. These advantages make TMR sensors particularly well-suited for biomagnetic measurement applications such as magnetocardiography (MCG), magnetomyography (MMG), magnetoencephalography (MEG) and Magnetoneurography (MNG) [1]–[15]. Biomagnetic signals typically lie in the femtotesla to picotesla range and are inherently weak, making them highly susceptible to environmental magnetic interference, as illustrated in Fig. 1(a) and summarized in Table I. Traditionally, biomagnetic measurements have relied on magnetic shielding to maintain ultra-low or near-zero field conditions. However, the growing demands for unshielded and ambient-field operation imposes stringent requirements on sensor system noise performance in the presence of strong background magnetic fields. This demand arises from the practical limitations of bulky shielding chambers in wearable, mobile or point-of-care settings, where form factor, cost, and usability are critical. Moreover, with the expanding variety of TMR sensors on the market, each exhibiting unique characteristics, it is crucial to establish comprehensive design guidelines to guide the development of interface circuits for accurate, low-power biomagnetic measurements.

A TMR sensor converts the amplitude and direction of a magnetic field into a corresponding linear resistance value. This transduction occurs through magnetic tunnel junctions (MTJs), which consist of multi-layer thin-film structures exhibiting quantum tunneling effects [16], [17]. These MTJs function as resistive elements whose values must be measured using an electronic interface circuit. We focus on the Wheatstone bridge, the most commonly used interface structure for measuring resistive sensors. This structure converts resistance variations into a differential voltage output, cancels DC offset, and minimizes thermal drift by rejecting common-mode resistance variations [18]. Various bridge configurations can be implemented, and Fig. 1(b) illustrates their structural arrangements along with the corresponding voltage output characteristics.

In an ideally balanced Wheatstone bridge, all four resistive elements are identical without an input signal, ensuring effective cancellation of power supply noise, which appears solely as a common-mode signal at the bridge's differential output. However, sensor mismatches can compromise the noise-rejection process, and allow supply noise to couple into the output [19]. This issue is particularly pronounced in ultra-

Manuscript received April 8, 2025; revised May 17, 2025 and June 1, 2025; accepted July 1, 2025. Date of publication July 10, 2025; date of current version July 31, 2025. (Dates will be inserted by IEEE; "published" is the date the accepted preprint is posted on IEEE Xplore®; "current version" is the date the typeset version is posted on Xplore®). Corresponding author: Hadi Heidari (e-mail: hadi@ neuranics.com).

Digital Object Identifier (inserted by IEEE).

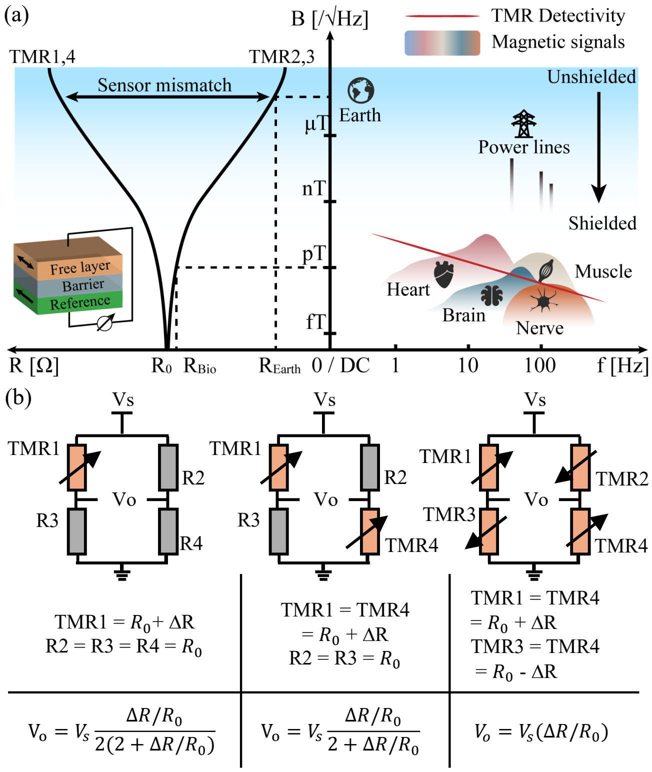

$$V_o = V_s \frac{\Delta R/R_0}{2(2+\Delta R/R_0)} \qquad V_o = V_s \frac{\Delta R/R_0}{2+\Delta R/R_0} \qquad V_o = V_s(\Delta R/R_0)$$

Fig. 1. (a) A summary of the spectral density of biomagnetic signals, noise and earth magnetic field in comparison to the detectivity and resistance changes of the TMR sensors. (b) The Wheatstone TMR bridge configurations (from left to right: quarter, half, and full) and their outputs.

sensitive TMR sensors with TMR ratios exceeding 100%, where large DC magnetic fields induce significant sensor mismatches (see Fig. 1(a)). As a result, operating in an unshielded environment can degrade the power supply rejection ratio (PSRR).

The voltage supplied to the Wheatstone bridge is a key factor in overall system performance, as it directly affects the output swing and power consumption. While low-voltage biasing (e.g., 0.4 V as reported in [8]) has been employed in some studies, higher voltages (e.g., 4 V in [10] and [20], and 1 V for [21]) are often used to enhance the output swing of the bridge. However, increasing the bias voltages can also introduce higher bias noise and greater power consumption, pushing the sensor closer to its breakdown voltage and thereby limiting its practical operating range. Hence, selecting an appropriate bias voltage is a critical design consideration.

The analog front-end (AFE) is another critical component of the electronic interface, as it must accurately amplify the small differential signals from the Wheatstone bridge while preserving the signal-to-noise ratio (SNR). As a result, the detection limit and resolution of the sensor system are ultimately constrained by the intrinsic noise of the TMR sensor bridge. To address this challenge, instrumentation amplifiers with high gain and excellent common-mode rejection ratios are typically used [10], [22]–[24], while additional filtering and chopping stages are used to further maintain the SNR [1], [10], [21], [25]–[28].

While prior studies have primarily focused on improving

TABLE I
NOISE FLOOR LIMITS FOR BIOMAGNETIC APPLICATIONS

Applications	Typical Frequency Band [Hz]	Signal Level	Detectivity Requirement$^{\alpha}$
MCG (Heart) [7]	0.05-150 Hz	Up to 100 pT	32 pT
MMG (Muscle) [8]-[10]	10-500 Hz	Up to 50 pT	16 pT
MEG (Brain) [11]-[12]	1-70 Hz	Up to 1 pT	300 fT
MNG (Nerve) [13]-[15]	10-5000 Hz	Up to 150fT	47 fT

$^{\alpha}$Assume maximum signal and the SNR is 10 dB.

individual components of the electronic interface, such as amplifier design or sensor biasing, they often lack a unified analysis that combines the TMR sensor behavior with practical system-level considerations. This paper presents a detailed analysis of the TMR sensor system through theoretical modeling and experimental validation of a TMR sensor manufactured by Neuranics Ltd. The study focuses on the effects of large DC magnetic fields on the PSRR and, ultimately, on sensor detectivity. Section II presents a comprehensive sensor model and theoretical analysis of various bridge configurations, establishing the fundamentals of PSRR and detectivity. Section III describes the hardware implementation, experimental setups and sensor characterization used to validate our theoretical model. Finally, Section IV presents the measurement results, thoroughly evaluating the detectivity and PSRR of the TMR sensor system.

II. THEORETICAL ANALYSES

The measurement system modeled in this study focuses on a Wheatstone bridge configuration that converts changes in magnetoresistance into a differential voltage output. A supply voltage powers the bridge V_{brigde}, such that when balanced, each TMR sensor is biased at $V_{TMR} = V_{brigde}/2$. The following subsections provide a detailed noise model of the TMR sensor, an analysis of various Wheatstone bridge configurations and their power supply rejection characteristics, and an evaluation of the overall system noise performance.

A. TMR Sensors Modeling

Each TMR sensor is assumed to consist of N MTJs connected in series, which improves its $1/f$ noise performance [29], with an average zero-field resistance r_0 per MTJ. The noise (n) power spectral density (PSD) is modeled with:

$$S_{V,n}^{TMR^2} = \frac{\alpha V_{TMR}^2}{NAf} + 2eV_{TMR}r_0 \cdot \coth\left(\frac{eV_{TMR}}{2Nk_BT}\right) \quad (1)$$

where α is Hooge's parameter, A is the section area, f is the frequency, e is the elementary charge, T the temperature, and k_B the Boltzmann constant[22], [29]–[31].

The first term in Eq. (1) represents $1/f$ noise. The Hooge's parameter, α, is an empirical constant characterizing 1/f noise in conductors and semiconductor devices. The second term in Eq. (1), expressed using the hyperbolic cotangent function, accounts for thermal (Johnson-Nyquist) noise. This expression is derived from physical shot noise models that incorporate thermal fluctuations in tunnel junctions, and has been widely adopted to describe noise behavior in MTJ-based devices. In the high-temperature or low-bias limit ($2Nk_BT \gg eV_{TMR}$), this term converges to the classical Johnson noise expression $4k_BTr_0$.

For a measurement bandwidth $[F_L, F_H]$, the RMS voltage noise is:

$$\mathrm{V}_{RMS,n}^{(\mathrm{F_L,F_H})} = \sqrt{\int_{F_L}^{F_H} S_{V,n}^{TMR}(f)^2 \; df}\,. \tag{2}$$

The equivalent noise magnetic field (detectivity) spectral density is then defined by:

$$S_{B,n} = \frac{S_{V,n}}{\mathrm{d}V/\mathrm{d}B} \tag{3}$$

where $\mathrm{d}V/\mathrm{d}B$ is the voltage sensitivity of the magnetic sensors system [29]. Finaly, the integrated RMS magnetic field noise is obtained by integrating $S_{B,n}$ over the bandwidth $[F_L, F_H]$.

B. Wheatstone Bridge Configuration

Fig. 1(b) shows three primary Wheatstone bridge configurations: quarter, half, and full. For biomagnetic signals, where $dR/R_0 \ll 2$, the outputs simplify to:

$$4 \cdot dV_o^{Quarter} = 2 \cdot dV_o^{Half} = dV_o^{Full} = V_s(\mathrm{d}R/R_0). \tag{4}$$

Note that the small resistance change ($\mathrm{d}R$) in the bridge is due to a small magnetic field change ($\mathrm{d}B$) and dR/dB is the resistance sensitivity of the TMR sensor. So that the voltage sensitivity ($\mathrm{d}V/\mathrm{d}B$) scales as:

$$dV_o^{Full}/dB = 2 \cdot dV_o^{Half}/dB = 4 \cdot \frac{dV_o^{Quarter}}{dB} \tag{5}$$

which indicates the full Wheatstone bridge configuration offers the highest sensitivity.

However, higher sensitivity does not necessarily lead to better detectivity, as the overall noise performance must also be considered. When evaluating different bridge configurations, the noise contributions from each of the four resistive elements in the Wheatstone bridge are assumed to be uncorrelated. The total output noise PSD of the bridge, expressed in the RMS domain, is therefore given by:

$$S_{V,n}^{Bridge^2} = N \cdot S_{V,n}^{TMR^2} + (4 - N) \cdot S_{V,n}^{R\;2} \tag{6}$$

where $S_{V,n}^R$ is the noise voltage spectral density of the fixed resistors in the bridge. Eq. (6) is derived by summing the uncorrelated noise contributions from all four resistive elements in the Wheatstone bridge. Here, N denotes the number of TMR sensors in the bridge, and $(4 - N)$ represents the number of fixed resistors. Since the noise sources are statistically independent, the total PSD of the bridge output noise can be expressed as the sum of their individual PSDs in the RMS domain. In the case where the $1/f$ noise from the TMR sensors dominates ($S_{V,n}^{TMR^2} \gg S_{V,n}^{R\;2}$), the overall noise scales approximately with the square root of the number of TMR sensors. Then it leads to:

$$S_{V,n}^{Full} = \sqrt{2} \cdot S_{V,n}^{Half} = 2 \cdot S_{V,n}^{Quarter}. \tag{7}$$

Substituting (5) and (7) into (3) yields the following detectivity relationships:

$$S_{B,n}^{Full} = 1/\sqrt{2} \cdot S_{B,n}^{Half} = 1/2 \cdot S_{B,n}^{Quarter}. \tag{8}$$

Thus, despite its higher voltage noise, the full Wheatstone bridge configuration offers superior sensitivity and improved detectivity. The full Wheatstone bridge output voltage is given by:

$$V_o = V_s(\Delta R/R_0^{TMR}) \tag{9}$$

where R_0^{TMR} is the zero-field resistance of a single TMR element in the bridge, and ΔR is the resistance changes due to the presence of the magnetic field B. To establish a more direct relationship between the magnetic field B and the output V_o, the resistive sensitivity dR/dB is introduced into Eq. (9), yielding the following expression:

$$V_o = V_s \cdot \frac{dR}{dB} \cdot \frac{B}{R_0^{TMR}}. \tag{10}$$

In this case, the output voltage increases with the supply voltage when other parameters are fixed. The voltage sensitivity, $\mathrm{d}V_o/\mathrm{d}B$ of the full Wheatstone TMR bridge can be derived as:

$$\mathrm{d}V_o/\mathrm{d}B = \frac{dR}{dB} \cdot \frac{V_s}{R_0^{TMR}} \tag{11}$$

and the normalized bridge sensitivity with respect to the supply voltage is given by:

$$S_S^{Bridge} = \frac{\mathrm{d}V_o/\mathrm{d}B}{V_S} = \frac{\mathrm{d}R}{\mathrm{d}B \cdot R_0^{TMR}}. \tag{12}$$

The unit for noirmalized bridge sensitivity S_S^{Bridge} is mV/V/mT.

C. Power Supply Rejection of the Wheatstone Bridge

An inherent advantage of the Wheatstone bridge is its ability to effectively reject supply noise (i.e., high PSRR). However, misalignment among TMR sensors and the presence of large DC magnetic fields cause resistance mismatch (ΔR_{mm}) which allows supply noise to couple into the output. With a non-ideal supply voltage $\mathrm{V_s} = \mathrm{V_{s,dc}} + \mathrm{V_{s,n}}$ (Eq. (13)), the output voltage in Eq. (9) becomes:

$$V_o = \frac{\mathrm{V_{s,dc}} \cdot \Delta R_{mm}}{R_0^{TMR}} + \frac{\mathrm{V_{s,n}} \cdot \Delta R_{mm}}{R_0^{TMR}} \tag{14}$$

where $\mathrm{V_{s,dc}}$ is the DC component of the voltage supply, and $\mathrm{V_{s,n}}$ is the AC noise component of the voltage supply. The first term in Eq. (14) can be filtered out by a high-pass filter, whereas the second term corresponds to wide-band supply noise coupled into the bridge output. With PSRR being the ratio of the noise in the supply voltage to the noise it produces at the bridge output, the PSRR can be expressed as:

$$\mathrm{PSRR} = \mathrm{V_{s,n}} / \frac{\mathrm{V_{s,n}} \cdot \Delta R_{mm}}{R_0^{TMR}}. \quad (15)$$

Incorporating the resistive sensitivity and expressing PSRR in decibels, it gives:

$$\mathrm{PSRR} = 20 \log_{10} \frac{R_0^{TMR}}{B_{DC} \cdot \mathrm{d}R/\mathrm{d}B}. \quad (16)$$

This equation demonstrates that PSRR deteriorates with increasing DC magnetic field, underscoring the necessity for a low-noise voltage regulator in high background magnetic fields.

D. Total measurement noise and detectivity

The overall noise comprises of contributions from the TMR sensor (in a full Wheatstone bridge configuration), supply noise, and AFE noise. As these three sources arise from independent physical origins—sensor junctions, power supply regulation, and amplifier electronics—they are treated as uncorrelated in the total noise model, and the total noise PSD is:

$$S_{V,n}^{Total^2} = S_{V,n}^{Bridge^2} + \left(PSRR \cdot S_{V,n}^{Supply}\right)^2 + S_V^{AFE^2} \quad (17)$$

where $S_{V,n}^{Supply^2}$ is the PSD of the bridge supply voltage noise and $S_V^{AFE^2}$ is that of the AFE, referred to as input (RTI). The RMS voltage noise over a measurement bandwidth $[\mathrm{F_L}, \mathrm{F_H}]$ is obtained by integrating the total noise PSD:

$$\mathrm{V}_{RMS,n}^{\mathrm{Total},[\mathrm{F_L},\mathrm{F_H}]} = \sqrt{\int_{F_L}^{F_H} S_{V,n}^{Total}(f)^2 \, df}. \quad (18)$$

Finally, the equivalent RMS magnetic field noise or detectivity is obtained by dividing $\mathrm{V}_{RMS,n}^{\mathrm{Total}}$ by $\mathrm{d}V/\mathrm{d}B$:

$$\mathrm{B}_{RMS,n}^{[\mathrm{F_L},\mathrm{F_H}]} = \frac{\mathrm{V}_{RMS,n}^{\mathrm{Total},[\mathrm{F_L},\mathrm{F_H}]}}{\mathrm{d}V/\mathrm{d}B}. \quad (19)$$

This analysis demonstrates that the minimum detectable magnetic field depends on the measurement bandwidth, sensor sensitivity, and noise contributions, including sensor intrinsic noise, AFE noise and those from the power supply, which vary with an external magnetic field. In subsequent sections, experimental validation of these theoretical predictions is presented, and the influence of different interfacing circuit designs on the overall noise performance is discussed.

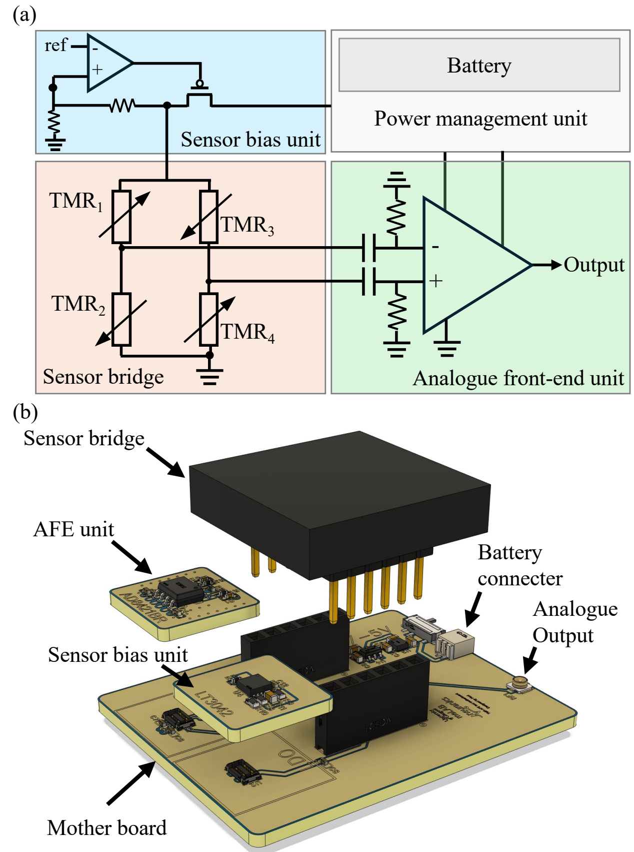

Fig. 2. The design of the Modular Experiments System (MES): (a) Schematic of the MES. (b) The structure of the MES.

III. Experiment Implementation

A. Modular experiments board design

To investigate the interaction of various noise sources and their impact on overall detectivity, we developed a Modular Experiments System (MES). As shown in Fig. 2(a), it comprises a sensor bias unit, an AFE unit, a TMR sensor bridge, and a motherboard. The motherboard is powered by a 3.7 V Lithium-ion battery and utilizes inductor-less charge pump regulators (LTC3204-5 and LTC1983-5 from Analog Devices) to generate a dual ±5 V supply, thereby minimizing electromagnetic interference (EMI) [32], [33]. In addition, it features interfaces for connecting functional units, sensor hosts, signal outputs, and the battery. This modular design facilitates measurement of different noise contributions and allows for the easy interchange of modules, thereby enabling comprehensive comparative studies of the various noise sources and their effects on overall system performance.

On the sensor bias unit, low-dropout (LDO) regulators were selected for their low-noise linear regulation compared to switching regulators (such as buck or boost converters). LDOs employ linear regulation, thereby minimizing high-frequency ripple and EMI, which might interfere with TMR sensors. Three low-noise LDOs were evaluated: LT3042 and LT3061 from Analog Devices and TPS7A9401 from Texas Instruments [34]–

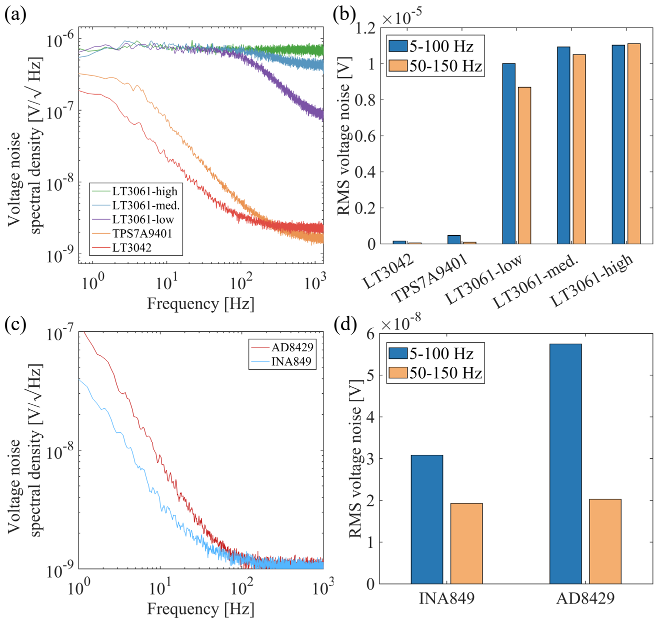

Fig. 3. Noise performance of the proposed daughter boards: (a) The noise voltage spectral density of different sensor bias units. (b) Integrated RMS noise of sensor bias units in different bandwidth (c) The voltage noise spectral density of AFE units. (d) Integrated RMS noise of AFE units in different bandwidth.

[36]. The LT3061's performance is tuned via its reference/bypass capacitor (C_{ref}) and the feedback capacitor (C_{ff}), with three configurations defined as LT3061-low (C_{ref}/ C_{ff} = 10/10 nF), LT3061-med (C_{ref}/ C_{ff} = 0.1/10 nF), and LT3061-high (C_{ref}/ C_{ff} = 0.1/0.1 nF). The LT3042 and TPS7A9401 boards were designed in strict accordance with the manufacturers' datasheets to ensure optimal performance. A bias voltage of 1 V was selected as it lies within the safe operating range of the sensor, provides sufficient excitation for signal detection, and facilitates straightforward comparison and normalization across configurations. Optimization of the supply voltage is further discussed in Section IV.C. Fig. 3(a) displays the measured noise spectral density of the LDO boards. Fig. 3(b) presents the corresponding RMS noise voltages calculated over the frequency bands of 5–100 Hz and 50–150 Hz. These two representative bands were selected to broadly assess the sensor system's noise performance across a range of frequencies commonly encountered in biomagnetic measurements. The 5–100 Hz band captures lower-frequency components that are typical in many biomagnetic signals, including those associated with cardiac and neurophysiological activity [37], [38]. Meanwhile, the 50–150 Hz band reflects higher-frequency dynamics relevant to applications such as magnetomyography (MMG), where muscle activity produces signal components extending into this range. [13], [39]. These bandwidths thus offer a practical framework for evaluating detectivity in diverse biomagnetic sensing scenarios. The LT3042 exhibits an RMS noise of 0.158 µV (5–100 Hz) and 0.058 µV (50–150 Hz), while the TPS7A9401 shows 0.467 µV and 0.094 µV, respectively. As anticipated, the LT3061 family demonstrates increased noise from the low-noise to the high-noise configuration, validating our design approach.

Each AFE board integrates a first-order high-pass filter and an instrumentation amplifier (INA) to condition the sensor bridge output. A high-pass filter with a 1 Hz cutoff was implemented before INA to attenuate near-DC signals that could saturate the amplifier and lie outside the biomagnetic signal bandwidth. INA was chosen as the amplification stage due to their high common-mode rejection ratio, high-input impedance and extremely low noise. Two low-noise INAs were evaluated: AD8429 (Analog Devices) and INA849 (Texas Instruments) [40], [41]. Both were set to have 60 dB gain. According to the datasheet, both have a white noise floor of 1 nV/√Hz when referred to the input, but their $1/f$ noise characteristics differ significantly. AD8429 exhibits higher current noise, which, combined with the resistor in the 1 Hz filter, results in elevated low-frequency noise. The measured noise voltage spectral density is shown in Fig. 3(c). Specifically, AD8429 shows an input-referred noise of 8.8 nV/√Hz at 10 Hz compared to 3.4 nV/√Hz for the INA849. RMS noise voltage measurements corroborate this difference: INA849 yields an RMS noise of 30 nV (5–100 Hz), whereas AD8429 registers 58 nV, as shown in Fig. 3(d).

The LDOs and instrumentation amplifiers selected in this study were chosen based on their low-noise performance, configurability, and potential suitability for low-power, scalable biomagnetic systems. Components such as the LT3042, TPS7A9401, INA849, and AD8429 represent commercially available options that allow for practical trade-off analysis in front-end design.

The MES was developed to enable flexible prototyping and comparative evaluation of analogue interface configurations. Although implemented with discrete components, the system architecture serves as a basis for future integration into compact or wearable platforms, where insights from this work will guide the use of integrated LDOs, layout optimization, and low-noise signal paths..

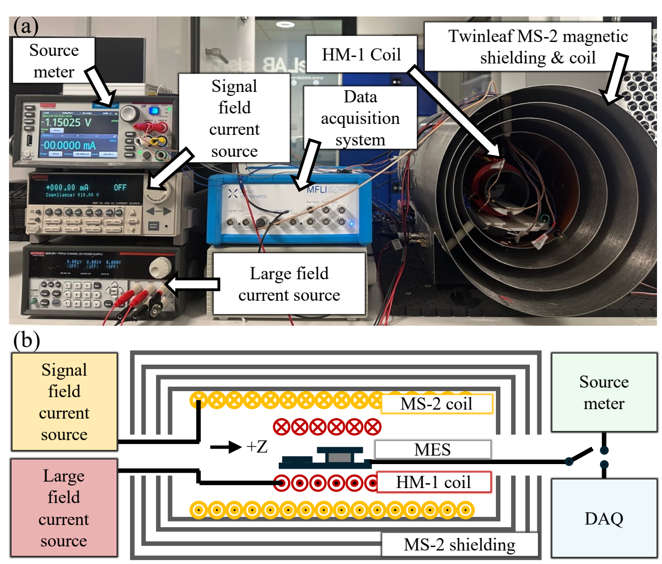

Fig. 4. Experimental setups: (a) Photography of the platform. (b) Schematic of the magnetic field generation and measurement setup.

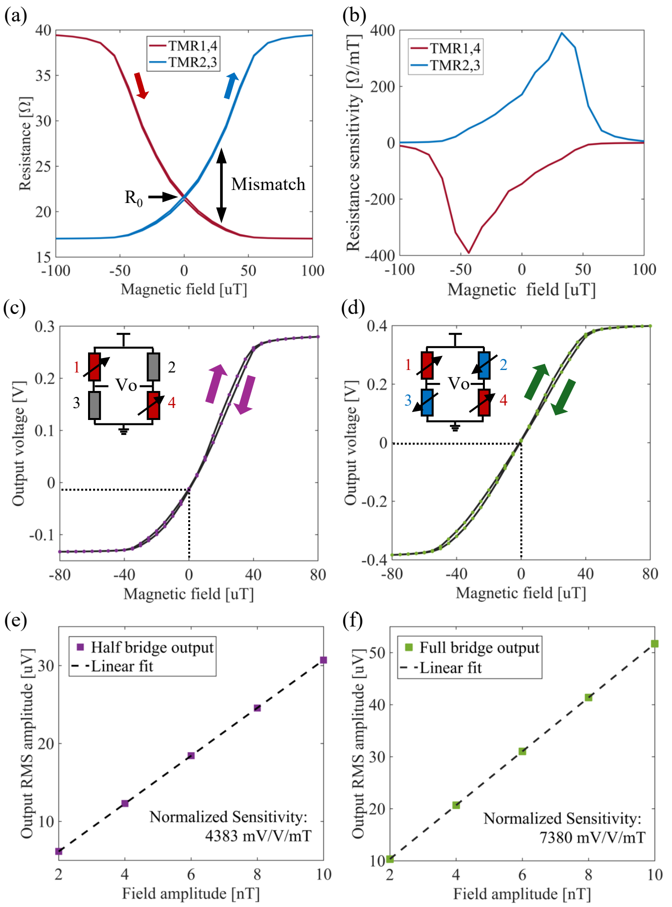

Fig. 5. Characterization results of the TMR sensor: (a) is the R-B curve of a single TMR sensor. (b) is the resistance sensitivity curve for a single TMR sensor. (c) and (d) is the V-B curves of the half and full Wheatstone bridge. (e) and (f) is the AC signal output of the half and full Wheatstone TMR sensor bridge.

B. Experimental platform

For accurate characterization of the TMR sensor system, a four-layer Twinleaf MS-2 magnetic shielding chamber [42] was used. The MS-2 chamber incorporates an embedded z-axis coil, and a secondary, custom-made coil (HM-1) generates large DC magnetic fields. Calibration of these coils is performed using a Fluxgate THM1176 [43], yielding a sensitivity of 159.5 nT/mA for the MS-2 coil and a sensitivity of 2550 nT/mA for the HM-1 coil. The MS-2 coil was driven by a Keithley 6221 current source to generate low-noise, small-amplitude magnetic fields. The HM-1 coil was controlled by a Keithley 2230 power supply to produce large DC fields.

A 3D-printed polylactic acid (PLA) holder positions the MES centrally, ensuring proper alignment with the coils and maximizing the shielding effect. The output from the MES is routed either to a Zurich Instruments MFLI for data acquisition or to a Keithley 2450 source meter for detailed sensor parameter characterization (including resistance and output voltage). Fig. 4(a) and 4(b) illustrate the experimental setup. This arrangement enables comprehensive evaluation of the system's behavior under varying DC magnetic fields and validation of the noise performance predicted by our theoretical model.

C. Sensors characterization

TMR sensors provided by Neuranics Ltd. can be configured as either half or full Wheatstone bridges. The sensor under investigation comprises 20 MTJs, each with a sectional area of 31416 um^2.

To assess the noise performance and PSRR of the sensor bridge, the resistance sensitivity (dR/dB) was first measured. These measurements were conducted within the MS-2 chamber under near-zero magnetic field conditions, using the HM-1 coil to generate a controlled magnetic field ranging from -100 uT to 100 uT in 10 uT increments, driven by a Keithley 2230 power supply. For resistance measurements, one TMR sensor was disconnected from the Wheatstone bridge and connected directly to a Keithley 2450 source meter, employing a four-terminal (Kelvin) technique to eliminate the meter's lead resistance and contact resistance errors. The measurement protocol involved a cyclic magnetic field sweep: starting at 0 mT, ramping to the positive maximum, descending to the negative maximum, and returning to 0 mT, with an initialization cycle preceding the data acquisition. At each magnetic field step, the field was held for 2 seconds, with resistance sampled during the final second at 10 Hz; the average of ten measurements was recorded. Fig. 5(a) presents the R-B curve, illustrating the sensor's resistance variation in response to the applied magnetic field. The zero-field resistance (R_0) was determined to be 21.5 Ω from the R-B curve of the TMR sensor. Since the sensor comprises 20 MTJs in series, the resistance of each MTJ under zero-field conditions (r_0) is estimated to be 1.075 Ω. Furthermore, the derivative of the R-B curve (Fig. 5(b)) indicates a resistive sensitivity of 171.5 Ω/mT near zero field.

Following resistance characterization, the sensor was re-integrated into half and full Wheatstone bridge configurations. The LT3042-based sensor bias unit, selected for its low noise performance, was used as the bridge supply. The bridge output was connected to the Keithley 2450, and the output voltage was measured while sweeping the magnetic field from –80 µT to 80 µT in 5 µT increments using the same protocol as for resistance measurement. The resulting data formed the voltage versus magnetic field curves (V-B curve) for the different bridge configurations, as shown in Fig. 5(c) and 5(d).

Finally, to characterize the AC sensitivity of the proposed Wheatstone sensor bridge, the bridge output was routed to the MES motherboard equipped with an INA849 AFE board, selected for its superior low-noise performance. The entire

TABLE II
SENSOR PARAMETERS IN MODELLING

Sensor parameter	Symbol	Value	Unit
MTJ section area	A	31416	um^2
MTJ number	N	20	-
MTJ zero-field resistance	r_0	1.075	Ω
Hooge's parameter	α	2.05×10^{-9}	um^2
Temperature	T	295	K
Elementary charge	e	1.6×10^{-19}	C
Resistive sensitivity	dR/dB	171.5	Ω/mT
Full-bridge voltage sensitivity	dV/dB	7380	mV/mT

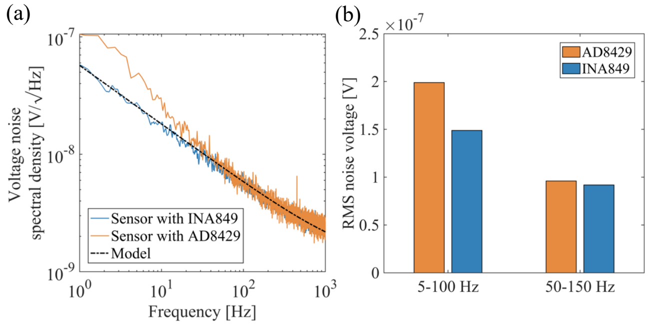

Fig. 6. Full Wheatstone sensor bridge noise performance: (a) Noise voltage spectral density of the bridge output with different amplifier-based AFE units. (b) The integrated RMS noise voltage within different bandwidth.

setup was placed inside the MS-2 chamber along with the magnetic coil. A sinusoidal magnetic field with an amplitude ranging from 2 nT to 10 nT was generated using a Keithley 6221 current source, and the output voltage from the MES motherboard was measured, as shown in Fig. 5(e) and 5(f). The bridge's voltage output was calculated by dividing the MES output voltage by the AFE gain. The results indicate an AC voltage sensitivity of 4383 mV/V/mT for the half-bridge and 7380 mV/V/mT for the full-bridge.

IV. Results and Discussion

A. AFE selection

A full Wheatstone bridge was connected to the MES using an LT3042 sensor bias unit along with different AFE units. The entire MES was positioned at the center of the MS-2 chamber, and all coil inputs were grounded to ensure that no external magnetic field was generated. As shown in Fig. 6(a), when the bridge output was connected to the AD8429-based AFE board, the sensor bridge exhibited a noise spectral density of 110 nV/√Hz at 1 Hz, whereas the INA849 configuration achieved a lower noise spectral density of 57 nV/√Hz. Considering that the intrinsic input-referred noise levels are 110 nV/√Hz for AD8429 and 38 nV/√Hz for INA849, the INA849-based AFE board reflects the intrinsic noise of the TMR sensor more accurately. Fig. 6(b) presents the RMS noise calculated over various frequency bands: in the 5–100 Hz range, AD8429 exhibited an RMS noise of 200 nV, compared to 149 nV for INA849; in the 50–150 Hz band, the RMS noise was 96 nV for AD8429 and 92 nV for INA849. These results clearly demonstrate that the AD8429 suffers from significantly higher noise in the low-frequency band. This direct comparison between two commercial INAs highlights the superior performance of INA849 and supports its selection for all subsequent experiments. Retaining the AD8429 data also enhances reproducibility and provides a reference point for alternative AFE designs. The calibrated Hooge's parameter was determined to be 2.05×10^{-9} μm². Table II summarizes the key sensor parameters used in the noise model. Incorporating these parameters into Eq. (1) yields the noise model shown as a dashed line in Fig. 6(a), which aligns well with the measured data using the INA849-based AFE board, thereby confirming the predictive accuracy of the noise model and underscoring the high fidelity of the experimental measurements. Consequently, all further experiments were conducted exclusively with the INA849-based AFE.

B. Bridge configurations

Both half and full Wheatstone bridge configurations were implemented to verify the modeling results. Fig 5(c) shows that the output of the half Wheatstone bridge exhibits 9% nonlinearity over a ±20 μT range, whereas the full Wheatstone bridge demonstrates only 4.3% nonlinearity over the same range (Fig. 5(d)). Additionally, the full-bridge output is more centered around zero, while the half-bridge output displays an offset. These V–B curve comparisons indicate that the full Wheatstone bridge configuration provides better linearity and reduced offset effects.

While the bridge maintains low noise performance in unshielded environments, the linearity of the sensor response can still degrade when subjected to strong background fields. This is because a large DC field shifts the sensor's operating point far from its nominal bias, especially in full-bridge configurations, which leads to response asymmetry and saturation effects. If precise linearity is required under such conditions, additional offset stabilization techniques such as magnetic field cancellation coils may be necessary [44].

The voltage noise of the TMR sensors in both configurations was measured in a near-zero field environment within the MS-2 chamber using the LT3042-based sensor bias unit and the INA849-based AFE. As depicted in Fig. 7(a), the recorded noise voltage spectral density is higher for the full Wheatstone bridge compared to the half Wheatstone bridge. Fig. 7 (c) shows

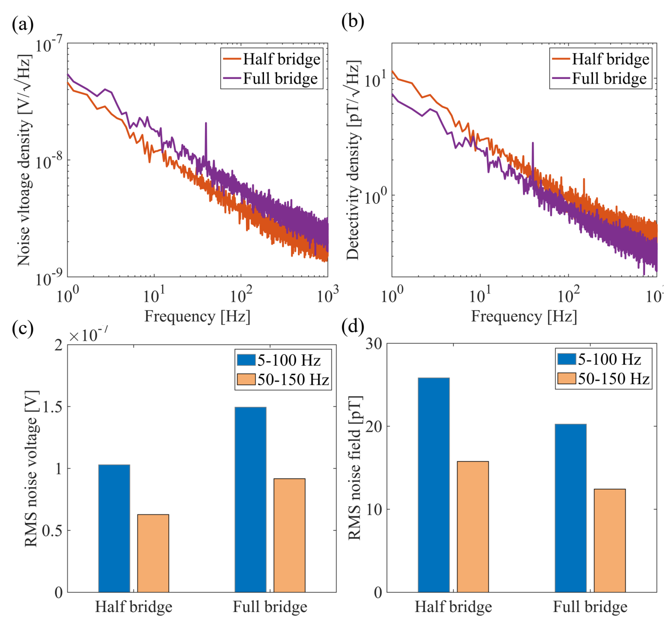

Fig. 7. Sensor noise performance in different bridge configurations: (a) Noise voltage spectral density of the half and full Wheatstone bridge configurations. (b) Detectivity spectral density of the half and full Wheatstone bridge configurations. (c) The integrated RMS noise voltage within different bandwidth. (d) The Field RMS noise within different bandwidth.

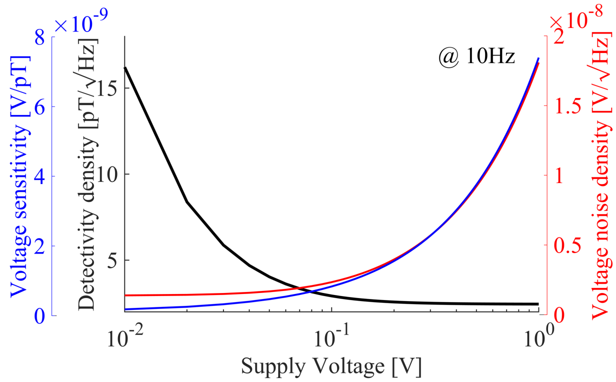

Fig. 8. Modeled detectivity, voltage sensitivity, and voltage noise spectral density of the full Wheatstone bridge as functions of supply voltage, evaluated at 10 Hz.

the integrated RMS noise over the 5–100 Hz and 50–150 Hz bands, confirming that the full Wheatstone bridge noise is approximately √2 times higher than that of the half Wheatstone bridge, consistent with the theoretical model.

Detectivity of the sensor bridge was computed using Eq. (3). With an AC sensitivity of 4383 mV/V/mT for the half Wheatstone bridge and 7380 mV/V/mT for the full Wheatstone bridge, the full Wheatstone bridge configuration exhibits approximately 1.7 times higher sensitivity than the half Wheatstone bridge. Although the theoretical model predicts a sensitivity ratio of 2, as derived in Eq. (5), where the full bridge output is expected to be twice that of the half bridge due to its symmetric differential configuration, the slight discrepancy may be attributed to misalignment of the TMR sensors in the full Wheatstone bridge, preventing it from reaching its maximum potential sensitivity. The detectivity results, shown in Fig. 7(d), indicate a detectivity of 7.4 pT/√Hz at 1 Hz for the full Wheatstone bridge and 11.4 pT/√Hz at 1 Hz for the half Wheatstone bridge. The integrated RMS noise over the 5–100 Hz band for the full Wheatstone bridge is 20.1 pT, which is sufficiently low for detecting the R peak in MCG [20]. In the 50–150 Hz band, the full Wheatstone bridge achieves an RMS noise of 12.6 pT, suggesting potential for MMG measurement [45]. In contrast, the half Wheatstone bridge exhibits RMS noise values of 26 pT and 16 pT in the 5–100 Hz and 50–150 Hz bands, respectively, making it less suitable for tracking MCG and MMG signals.

C. Supply voltage of TMR sensor

Our theoretical model enables the optimization of the supply voltage for the TMR sensor bridge, specifically at a measurement frequency of 10 Hz. As indicated by Eq. (6), the noise voltage spectral density for a full Wheatstone bridge is $\sqrt{2} \cdot S_{V,n}^{TMR}$, where $S_{V,n}^{TMR}$ is defined in Eq. (1) using parameters from Table. 1. Fig. 8 (red curve) shows that the noise voltage spectral density at 10 Hz increases with the supply voltage. In parallel, the voltage sensitivity of the full Wheatstone bridge (as given by Eq. (11)) also increases with the supply voltage, as shown by the blue curve in Fig. 8. However, these increases do not scale proportionally. When these effects are combined via Eq. (3), the detectivity density at 10 Hz improves—that is, the minimum detectable field decreases—with increasing supply voltage, as indicated by the black curve in Fig. 8. Notably, the detectivity converges to approximately 2.5 pT/√Hz beyond 0.1 V, indicating that further increases in the supply voltage do not yield significant improvements on detectivity. For an optimal AFE design, it is crucial to ensure that the AFE's RTI noise remains lower than the sensor bridge output noise, a condition that can be achieved by appropriately adjusting the supply voltage. Fig. 8 also indicates that an optimal supply voltage can be identified from a power consumption standpoint. Specifically, although increasing the supply voltage initially improves the detectivity by enhancing the bridge's voltage sensitivity relative to its noise, further increases beyond approximately 0.1 V yield only marginal detectivity improvements while significantly increasing power consumption. This observation underscores the need for a balanced design strategy that optimizes both performance and energy efficiency in practical sensor applications.

D. Detectivity with different LDOs

To assess the impact of different LDOs on the detectivity of the TMR sensor bridge under varying background magnetic fields, the sensor bridge was centrally positioned within MS-2 magnetic shielding chamber equipped with calibrated coils. LDOs were sequentially connected to the motherboard, and detectivity was evaluated under two conditions: (i) near-zero field (0 µT) with no current in the HM-1 coil, and (ii) under a large DC background field applied via an external current source.

Fig. 9(a) and 9(b) illustrate the field noise spectrum densities measured under these conditions. At near-zero field, all LDOs exhibited similar spectra. However, when a 5 µT background field was applied, marked differences emerged. Specifically, for the LT3061 family, the field noise spectrum closely followed the intrinsic voltage noise characteristics of the LDO,

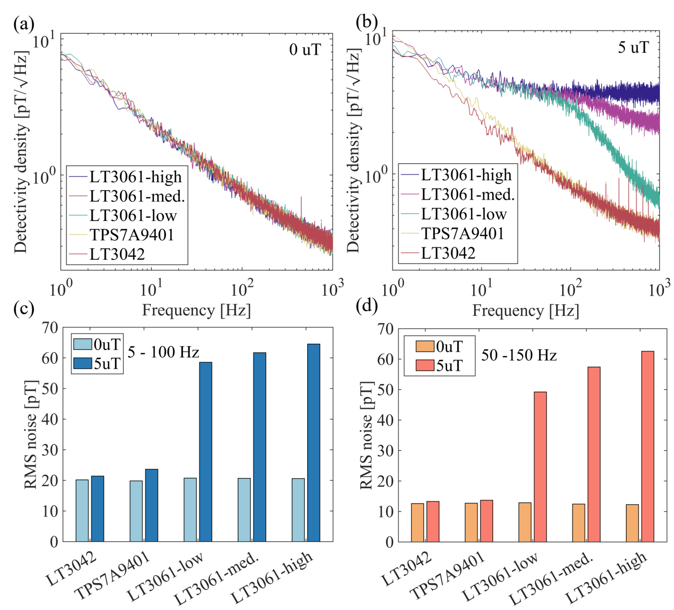

Fig. 9. Noise performance of different LDOs: (a) Detectivity spectral density under 0 µT. (b) Detectivity spectral density under 5 µT magnetic field. (c) Field RMS noise of LT3061-high under different magnetic field noise within different bandwidth. (d) Field RMS noise within 5-100 Hz.

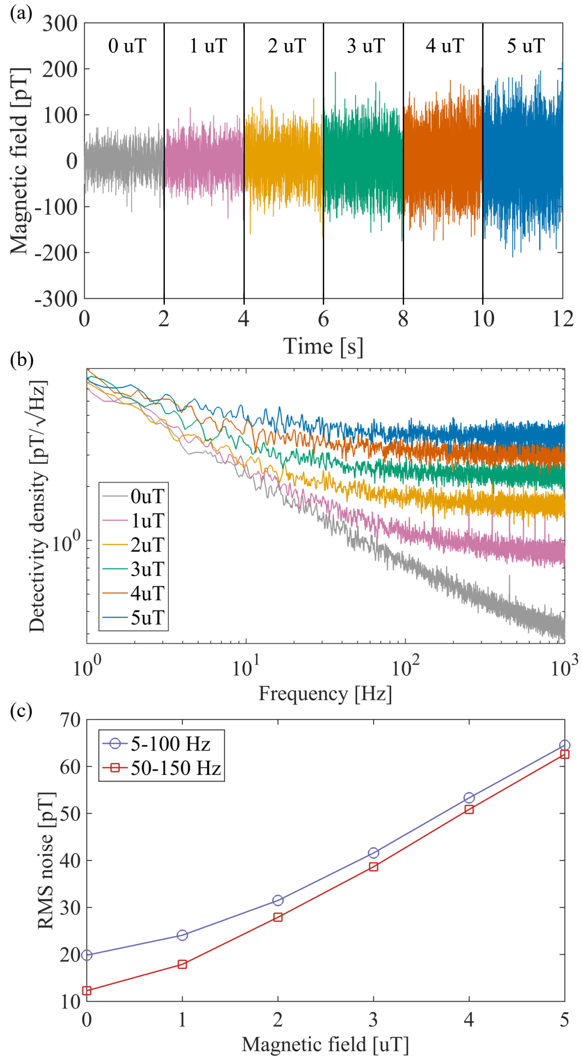

Fig. 10. Equivalent field noise (detectivity) when supplied with LT3061-high under 0-5 μT magnetic field: (a) Time recorded data within bandwidth of 1-1000 Hz. (b) Detectivity spectral density. (c) RMS field noise within different bandwidth.

while sensor bridges powered by the TPS7A9401 and LT3042 showed only minor increases—indicating effective noise suppression by these regulators.

For quantitative analysis, the RMS field noise was computed over the 5–100 Hz and 50–150 Hz frequency bands using Eq. (19). As shown in Fig. 9(c) and 9(d), under near-zero field conditions, the RMS field noise was approximately 20 pT in the 5–100 Hz band and 12 pT in the 50–150 Hz band across all LDOs. Under a 5 μT background field, the RMS field noise for the LT3061 family increased significantly—from around 20 pT to 60 pT in the 5–100 Hz band—exceeding the noise floor typically needed for reliable detection of cardiac-related signals such as MCG R-peaks. In contrast, the LT3042 and TPS7A9401 configurations exhibited only modest increases, reaching 21 pT and 23 pT, respectively. In the 50–150 Hz band, the LT3061 configurations yielded RMS field noise values of 49 pT, 57 pT, and 62 pT for the low, medium, and high noise configurations, respectively, while LT3042 and TPS7A9401 increases were limited to 5.6% and 8.5% (from 12.6 pT to 13.3 pT and 12.7 pT to 13.7 pT, respectively). The difference between the LT3061-low and LT3061-high configurations—12% in the 5–100 Hz band and 27% in the 50–150 Hz band—further confirms that the LT3061-high setup exhibits significantly higher high-frequency noise components, in line with our voltage noise measurements of LDOs.

Furthermore, by connecting the LT3061-high LDO to the motherboard and sweeping the background field from 0 μT to 5 μT using the HM-2 coil, we recorded the sensor bridge voltage noise. We calculated the detectivity based on the measured sensitivity. Fig. 10(a) shows the recorded noise field data in a time series, with a simple filter applied to the range of 1-1000 Hz, clearly illustrating the increase in noise. For quantitative analysis, Fig. 10(b) and 10(c) depict the evolution of the field noise spectrum and the corresponding RMS field noise, clearly showing that the RMS field noise increases from 20 pT to 64 pT in the 5–100 Hz band and from 12 pT to 62 pT in the 50–150 Hz band as the background field increases.

E. PSRR of the bridge

To investigate the origin of the observed noise increase, it is attributed to a degradation in the bridge's PSRR, as formulated in Eq. (17). As established in Section IV.A, the use of the INA849 amplifier allows for accurate measurement of the intrinsic noise of the sensor bridge. Therefore, the contribution of the AFE noise, S_V^{AFE} can be reasonably neglected in the analysis. In this context, the RMS voltage noise of the LDO is denoted as $\mathrm{V}_{RMS,n}^{\mathrm{LDO}}$, the RMS voltage noise of the sensor bridge under near-zero magnetic field is denoted as $\mathrm{V}_{RMS,n_0}^{\mathrm{Bridge}}$, and the RMS voltage noise under a non-zero applied DC magnetic field is denoted as $\mathrm{V}_{RMS,n}^{\mathrm{Total}}$. Substituting these measured values into Eq. (17), the PSRR can be experimentally determined using the following expression:

$$\mathrm{PSRR} = \sqrt{\frac{{\mathrm{V}_{RMS,n}^{\mathrm{Total}}}^{2} - {\mathrm{V}_{RMS,n_0}^{\mathrm{Bridge}}}^{2}}{{\mathrm{V}_{RMS,n}^{\mathrm{LDO}}}^{2}}}. \quad (20)$$

We computed the PSRR over two frequency ranges, 5–100 Hz and 50–150 Hz, with the results presented in Fig. 11. The model prediction, calculated using Eq. (16), is shown as the dotted line in Fig. 11. Under near-zero magnetic field conditions (0 μT), the modeled PSRR exceeds 60 dB, representing an ideal scenario where all TMR sensors exhibit identical zero-field resistance; the measured data also indicate an infinite |PSRR| at 0 μT, which are therefore not shown in the

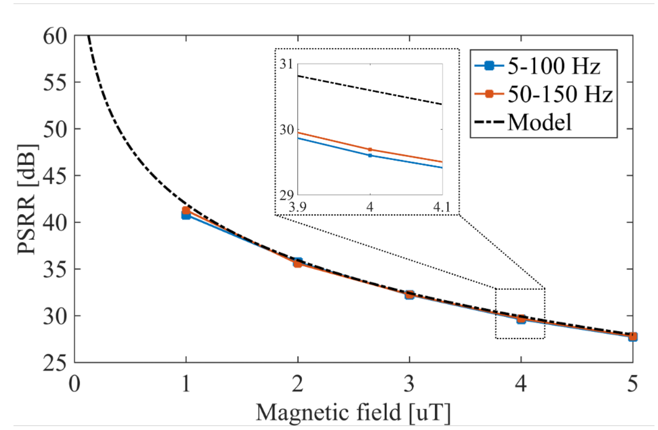

Fig. 11. PSRR calculation with different bandwidth.

TABLE III
COMPARISON AGAINST THE STATE OF THE ART

	Bridge config.	Bias voltage [V]	Bias noise$^{\alpha}$ [nV/√Hz]	AFE noise$^{\alpha}$ [nV/√Hz]	Shielded env.	Detect.$^{\alpha}$ [pT/√Hz]
JSSC'21 [28]	Quarter	-	13^{β}	15^{β}	-	$10^{4\,\beta}$
SSCL'22 [21]	Quarter	1.4^{β}	3^{β}	60^{β}	Yes	658^{β}
Sensors'22 [5]	Full	4	-	1.8^{β}	No	500^{β}
Sci.Rep.'22 [3]	Quarter	0.4	-	-	Yes	0.1^{β}
TIM'23 [24]	Full	1^{β}	25^{β}	43	-	$20^{6\,\beta}$
This work	**Full**	**1**	**3**	**1.2**	**No**	**0.79**

$^{\alpha}$At 100 Hz. $^{\beta}$Estimated from figures and text.

figure. Specifically, at 1 µT, the measured |PSRR| is approximately 40 dB, dropping to less than 30 dB at 5 µT. This reduction in PSRR indicates that as the DC magnetic field increases, the degraded rejection allows a larger fraction of the LDO's inherent noise to couple into the bridge output. Consequently, the noise performance of the LDO becomes increasingly critical, as stronger external magnetic fields demand superior noise suppression to preserve the sensor system's overall detectivity.

The inset of Fig. 11 provides a detailed view around 4 µT, clearly showing minimal variation in PSRR across the two frequency bands. A lower |PSRR| in the low-frequency band suggests that additional noise sources--such as amplifier noise—may be coupling into the bridge output. This is supported by the increased INA849 amplifier noise at low frequencies, which approaches the measured bridge noise. Notably, the theoretical model consistently predicts higher |PSRR| values than those measured experimentally. This discrepancy is likely due to intrinsic mismatches and misalignment among the TMR elements in the Wheatstone bridge, resulting from fabrication tolerances and manual assembly.

While this study is based on a TMR sensor with fully characterized internal parameters, the methodology is not limited to this specific device**.** Beyond the specific sensor studied, the proposed design methodology is adaptable to a broader range of commercial TMR sensors, including those with undisclosed structural details such as MTJ count or junction area. In these cases, Eq. (1) can be applied as a generalized form, where the composite term $\alpha/(N \cdot A)$ is empirically extracted from the measured voltage noise spectral density. This approach enables accurate modeling of the sensor's noise behavior without requiring access to its internal physical design. Once calibrated, these parameters can be directly incorporated into the same analytical framework to predict detectivity, PSRR variation, and system-level performance. Combined with the modular structure of the proposed experimental platform, this framework allows for fast adaptation to a wide range of TMR sensors and provides practical design guidance for engineers developing precision biomagnetic sensing systems.

In summary, the experimental trend of decreasing PSRR with increasing background magnetic field is consistent with model predictions, confirming that LDO noise becomes the dominant factor in bridge output noise under such conditions. These findings reinforce the accuracy of the proposed analytical model in capturing system-level behavior. Although this study focuses primarily on electrical and magnetic factors affecting PSRR and detectivity, it should be noted that environmental influences such as temperature drift and mechanical vibration may further degrade bridge balance and exacerbate the coupling of power supply noise, particularly in unshielded settings.

In this study, the observed degradation in PSRR is primarily attributed to field-induced mismatch among TMR elements in the full Wheatstone bridge, which increases with the applied DC magnetic field. To mitigate this effect, one practical approach is to apply a feedback coil to stabilize the operating point of each sensor, thereby maintaining bridge symmetry under varying field conditions.

Fabrication-related mismatches, such as angular misalignment or resistance variation across sensor elements, can further affect PSRR, especially in large-scale production. These effects can be minimized by monolithically integrating multiple TMR elements with predefined inversed sensitivity directions on the same die. This strategy has been demonstrated to reduce alignment error and ensure tighter performance matching, while remaining scalable for high-volume manufacturing.

Table III compares the circuit setup in this work to the state-of-the-art in MR electronic interfaces. Compared with existing studies that individually address circuit design or sensor modeling, the methodology proposed in this work emphasizes the interplay between TMR sensor characteristics, power supply behavior, and analogue front-end performance under varying field conditions. This integrated perspective not only enables more accurate detectivity prediction but also provides practical design guidance that bridges theoretical modeling with real-world implementation constraints.

V. CONCLUDING REMARKS

In this work, a comprehensive investigation of the electronic interface design for ultra-sensitive TMR sensors in biomagnetic field measurements was presented. The study systematically evaluated key design factors—including sensor parameters, Wheatstone bridge configurations, sensor supply optimization, and AFE noise performance—to determine their impact on system detectivity. The analysis indicates that among the various bridge configurations evaluated, the full Wheatstone bridge yields superior detectivity and linearity. Furthermore, optimal performance requires that the AFE maintains voltage noise levels below the sensor's intrinsic noise—especially within the $1/f$ noise region. Additionally, the study demonstrates that optimizing the sensor supply voltage is essential for balancing performance enhancements with power consumption. Further evaluation of bridge performance under varying large DC magnetic fields highlighted that LDO noise becomes a critical factor, as degradation of the bridge's PSRR allows an increasing portion of LDO noise to couple into the output. This, in turn, limits the overall noise floor and detectivity of the system. The insights gained from both noise modeling and experimental evaluations validate the design choices made for the AFE and provide clear guidelines for future improvements in sensor integration and noise suppression. Furthermore, even when the detailed internal parameters of a TMR sensor are unavailable, the proposed noise modeling framework can still be applied by empirically extracting composite parameters from spectral measurements, thereby ensuring the methodology's adaptability to a wide range of commercial sensors. The modular system architecture and findings from this study offer a solid foundation for future integration into wearable or chip-scale implementations, where power and noise constraints remain critical.

While this study primarily focuses on characterizing and mitigating electrical noise sources, it is acknowledged that environmental factors such as temperature fluctuations and mechanical vibrations may further affect bridge balance and PSRR, particularly in unshielded environments. These influences were not explicitly modeled or tested in the present work. Future studies will aim to incorporate environmental robustness strategies, including thermal drift compensation and mechanical isolation, to enhance system stability and reliability under practical operating conditions.

Overall, the work establishes a practical, generalizable framework for the electronic interface design of TMR-based sensing systems, paving the way for high-sensitivity biomagnetic applications that can be operated without extensive magnetic shielding.

Acknowledgment

This work was supported partially by the UK EPSRC under Grant EP/X031950/1 SUPREMISE project.

References

[1] S. Zuo, H. Heidari, D. Farina, and K. Nazarpour, 'Miniaturized Magnetic Sensors for Implantable Magnetomyography', *Adv. Mater. Technol.*, vol. 5, no. 6, 2020.

[2] H. Wang, S. Zuo, M. Cerezo-Sánchez, N. G. Arekhloo, K. Nazarpour, and H. Heidari, 'Wearable super-resolution muscle–machine interfacing', *Front. Neurosci.*, vol. 16, no. November, pp. 1–23, 2022.

[3] M. Hämäläinen, R. Hari, R. J. Ilmoniemi, J. Knuutila, and O. V. Lounasmaa, 'Magnetoencephalography—theory, instrumentation, and applications to noninvasive studies of the working human brain', *Rev. Mod. Phys.*, vol. 65, no. 2, pp. 413–497, Apr. 1993.

[4] J. Velmurugan, S. Sinha, and P. Satishchandra, 'Magnetoencephalography recording and analysis', *Ann. Indian Acad. Neurol.*, vol. 17, no. SUPPL. 1, 2014.

[5] Y. Bu *et al.*, 'Peripheral Nerve Magnetoneurography With Optically Pumped Magnetometers', *Front. Physiol.*, vol. 13, no. March, 2022.

[6] I. Ozaki, M. Akaza, T. Watanabe, Y. Miyano, Y. Adachi, and S. Kawabata, 'Detailed magnetoelectric analysis of a nerve impulse propagation along the brachial plexus', *Clin. Neurophysiol.*, vol. 145, pp. 129–138, 2023.

[7] M. Burghoff, B. M. Mackert, W. Haberkorn, G. Curio, and L. Trahms, 'High-resolution magnetoneurography', *Appl. Supercond.*, vol. 6, no. 10–12, pp. 567–575, 1999.

[8] A. Kanno *et al.*, 'Scalp attached tangential magnetoencephalography using tunnel magneto-resistive sensors', *Sci. Rep.*, vol. 12, no. 1, pp. 1–9, Apr. 2022.

[9] K. D. Bergmeister, S. Salminger, and O. C. Aszmann, 'Targeted Muscle Reinnervation for Prosthetic Control', *Hand Clin.*, vol. 37, no. 3, pp. 415–424, 2021.

[10] W. Zhao, X. Tao, C. Ye, and Y. Tao, 'Tunnel Magnetoresistance Sensor with AC Modulation and Impedance Compensation for Ultra-Weak Magnetic Field Measurement', *Sensors*, vol. 22, no. 3, p. 1021, Jan. 2022.

[11] J. Amaral *et al.*, 'Integration of TMR sensors in silicon microneedles for magnetic measurements of neurons', *IEEE Trans. Magn.*, vol. 49, pp. 3512–3515, 2013.

[12] T. Elfouly and A. Alouani, 'Harnessing the Heart's Magnetic Field for Advanced Diagnostic Techniques', *Sensors*, vol. 24, no. 18, 2024.

[13] N. Ghahremani Arekhloo *et al.*, 'Alignment of magnetic sensing and clinical magnetomyography', *Frontiers in Neuroscience*, vol. 17. Frontiers Media S.A., 2023.

[14] M. Kruse *et al.*, 'Magnetic vector field mapping of the stimulated abductor digiti minimi muscle with optically pumped magnetometers', *Biomed. Phys. Eng. Express*, vol. 11, no. 2, p. 025028, Mar. 2025.

[15] J. von Fraunberg *et al.*, 'Facial magnetomyography using an array of optically pumped magnetometers', *Clin. Neurophysiol. Pract.*, vol. 10, no. March, pp. 134–140, 2025.

[16] P. P. Freitas, R. Ferreira, and S. Cardoso, 'Spintronic Sensors', *Proc. IEEE*, vol. 104, no. 10, pp. 1894–1918, Oct. 2016.

[17] F. Favita, P. D. R. Araujo, F. Matos, S. Cardoso, and P. P. Freitas, 'Evaluation of the feasibility of TMR sensor array vertical packing for enhanced detectivity', *IEEE Trans. Magn.*, 2025.

[18] S. Zuo, H. Fan, K. Nazarpour, and H. Heidari, 'A CMOS analog front-end for tunnelling magnetoresistive spintronic sensing systems', *Proc. - IEEE Int. Symp. Circuits Syst.*, vol. 2019-May, no. February, pp. 26–29, 2019.

[19] J. Van Rethy, H. Danneels, V. De Smedt, W. Dehaene, and G. E. Gielen, 'Supply-noise-resilient design of a bbpll-based force-balanced wheatstone bridge interface in 130-nm cmos', *IEEE J. Solid-State Circuits*, vol. 48, no. 11, pp. 2618–2627, 2013.

[20] K. Fujiwara *et al.*, 'Magnetocardiography and magnetoencephalography measurements at room temperature using tunnel magneto-resistance sensors', *Appl. Phys. Express*, 2018.

[21] A. Mohamed, M. Wagner, H. Heidari, and J. Anders, 'A Frontend for Magnetoresistive Sensors With a 2.2-pA/√Hz Low-Noise Current Source', *IEEE Solid-State Circuits Lett.*, vol. 5, pp. 17–20, 2022.

[22] S. Cardoso *et al.*, 'Magnetic tunnel junction sensors with pTesla sensitivity', in *Microsystem Technologies*, 2014, vol. 20, no. 4–5, pp. 793–802.

[23] W. Zhang *et al.*, 'A low noise CMOS instrumentation amplifier for TMR-effect-based magnetic sensors', *Mod. Phys. Lett. B*, vol. 35, no. 12, p. 2150178, Apr. 2021.

[24] J. Liu *et al.*, ‘Enhanced Limit-of-Detection of Current Sensor Based on Tunneling Magnetoresistive Effect With Multichips Differential Design’, *IEEE Trans. Instrum. Meas.*, vol. 72, 2023.
[25] S. Zuo, K. Nazarpour, and H. Heidari, ‘High-precision biomagnetic measurement system based on tunnel magneto-resistive effect’, *ICECS 2020 - 27th IEEE Int. Conf. Electron. Circuits Syst. Proc.*, pp. 8–11, 2020.
[26] H. Wang *et al.*, ‘Study of Chopping Magnetic Flux Modulation on Surface Acoustic Wave Magnetic Sensor’, *ICECS 2022 - 29th IEEE Int. Conf. Electron. Circuits Syst. Proc.*, 2022.
[27] V. L. Su, J. T. Jeng, J. H. Hsu, C. R. Chang, and C. C. Lu, ‘Tunneling-Magnetoresistance Vector Magnetometer with Deflection Flux-Chopper’, *IEEE Trans. Magn.*, vol. 52, no. 7, pp. 1–4, 2016.
[28] X. Zhou *et al.*, ‘A 9.7-nT, 704-ms Magnetic Biosensor Front-End for Detecting Magneto-Relaxation’, *IEEE J. Solid-State Circuits*, vol. 56, no. 7, pp. 2171–2181, Jul. 2021.
[29] R. Guerrero, M. Pannetier-Lecoeur, C. Fermon, S. Cardoso, R. Ferreira, and P. P. Freitas, ‘Low frequency noise in arrays of magnetic tunnel junctions connected in series and parallel’, *J. Appl. Phys.*, vol. 105, no. 11, p. 113922, Jun. 2009.
[30] E. Paz, S. Serrano-Guisan, R. Ferreira, and P. P. Freitas, ‘Room temperature direct detection of low frequency magnetic fields in the 100 pT/Hz0.5 range using large arrays of magnetic tunnel junctions’, *J. Appl. Phys.*, vol. 115, no. 17, p. 17E501, Jan. 2014.
[31] W. F. Egelhoff *et al.*, ‘Critical challenges for picoTesla magnetic-tunnel-junction sensors’, *Sensors Actuators A Phys.*, vol. 155, no. 2, pp. 217–225, Oct. 2009.
[32] ‘LTC3204’, *Analog Devices*. [Online]. Available: https://www.analog.com/en/products/ltc3204.html.
[33] ‘LTC1983’, *Analog Devices*. [Online]. Available: https://www.analog.com/en/products/ltc1983.html.
[34] ‘LT3042’, *Analog Devices*. [Online]. Available: https://www.analog.com/media/en/technical-documentation/data-sheets/3042fb.pdf. [Accessed: 01-Mar-2025].
[35] ‘LT3061’, *Analog Devices*. [Online]. Available: https://www.analog.com/media/en/technical-documentation/data-sheets/3061fb.pdf. [Accessed: 01-Mar-2025].
[36] ‘TPS7A9401’, *Texas Instruments*. [Online]. Available: https://www.ti.com/lit/ds/symlink/tps7a94.pdf. [Accessed: 01-Mar-2025].
[37] M. Oogane *et al.*, ‘Sub-pT magnetic field detection by tunnel magneto-resistive sensors’, *Appl. Phys. Express*, vol. 14, no. 12, p. 123002, Nov. 2021.
[38] L. G. Tereshchenko and M. E. Josephson, ‘Frequency content and characteristics of ventricular conduction’, in *Journal of Electrocardiology*, 2015, vol. 48, pp. 933–937.
[39] T. Klotz, L. Gizzi, and O. Röhrle, ‘Investigating the spatial resolution of EMG and MMG based on a systemic multi-scale model’, *Biomech. Model. Mechanobiol.*, vol. 21, no. 3, pp. 983–997, 2022.
[40] ‘AD8429’, *Analog Device*. [Online]. Available: https://www.analog.com/media/en/technical-documentation/data-sheets/AD8429.pdf. [Accessed: 01-Mar-2025].
[41] ‘INA849’, *Texas Instruments*. [Online]. Available: https://www.ti.com/lit/ds/symlink/ina849.pdf. [Accessed: 01-Mar-2025].
[42] ‘MS-2 Magnetic shield’. [Online]. Available: https://twinleaf.com/shield/MS-2/. [Accessed: 28-Feb-2025].
[43] ‘Three-Axis Hall Effect Magnetometer THM1176 - MetroLab’. [Online]. Available: https://www.metrolab.com/products/three-axis-hall-effect-magnetometer-thm1176/. [Accessed: 28-Feb-2025].
[44] K. Kurashima *et al.*, ‘Development of Magnetocardiograph without Magnetically Shielded Room Using High-Detectivity TMR Sensors’, *Sensors*, vol. 23, no. 2, p. 646, Jan. 2023.
[45] S. Nordenström *et al.*, ‘Feasibility of magnetomyography with optically pumped magnetometers in a mobile magnetic shield’, *Sci. Reports 2024 141*, vol. 14, no. 1, pp. 1–10, Aug. 2024.

Huxi Wang received dual B.Eng. degrees in Electrical and Electronics Engineering from the University of Glasgow, UK, and the University of Electronic Science and Technology of China (UESTC), China, in 2020. He is currently pursuing a Ph.D. at the University of Glasgow, focusing on the development of ultra-sensitive TMR sensor systems. In 2021, he was awarded a fellowship from CRC1261 at Kiel University, Germany. His Ph.D. research has successfully transitioned into the startup company, Neuranics, where he now works as a sensor engineer. His research interests include measurement technology, magnetic sensor applications and deep-space technology.

Meraj Ahmad received the M.Tech + Ph.D. (Dual Degree) from the Indian Institute of Technology Bombay in 2021. He is currently a Post-Doctoral Research Associate at the University of Glasgow, UK, and a Senior Analog/Mixed-Signal IC Design Engineer at Neuranics. His research interests include analog circuit design and embedded system design for sensing applications.

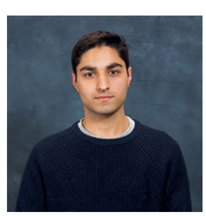

Asfand Tanwear received his M.Eng. (2018) and Ph.D. (2023) degrees both from the University of Glasgow. He studied electrical and electronics engineering followed by a PhD looking into spintronic sensors based on magnetic tunnel junction for Wearable Applications. He is now a senior sensor engineer at Neuranics, specializing in designing and fabricating ultra-low noise spintronic magnetic sensors for biomagnetic field application.

Negin Ghahremani Arekhloo received her medical degree from Shiraz University of Medical Science (SUMS), Iran, in 2020. He is currently pursuing a Ph.D. in Electrical and Electronics Engineering at the University of Glasgow, focusing on Biomagnetic measurements using quantum sensors, particularly TMR sensors. She is also a clinical scientist at Neuranics Limited, a deep-tech company specializing in scalable TMR quantum sensing solutions. Her research involves biomagnetic experiments and the development of magnetic sensor applications, with a focus on magnetocardiography, magnetomyography, and gesture tracking using magnetic sensors.

Siming Zuo received his B.Eng. and Ph.D. degrees both in Electrical and Electronics Engineering at the University of Electronic Science & Technology of China (UESTC), China in 2017 and at the University of Glasgow in 2021. He is currently a Co-Founder and Lead Engineer at Neuranics Limited, a deep-tech company specializing in scalable TMR quantum sensing solutions. He has authored and co-authored over 40 peer-reviewed publications in top-tier journals or conference proceedings and filed 2 international patents. His research interests include microelectronics and magnetic sensor technologies for human-machine interfaces in healthcare, education, consumer electronics, metaverse, gaming markets and many others.

Kianoush Nazarpour (S'05–M'08–SM'14) received the B.Sc. degree from K.N. Toosi University of Technology, Tehran, Iran, in 2003, the M.Sc. degree from Tarbiat Modarres University, Tehran, Iran, in 2005, and the Ph.D. degree from Cardiff University, Cardiff, U.K., in 2008, all in electrical and electronic engineering. He is now a Professor of Digital Health at The University of Edinburgh and Co-Founder and Chief Strategy Officer at Neuranics Limited. His research interests include digital health and care, AI-enabled wearables, neural systems and rehabilitation engineering.

Hadi Heidari (Senior Member, IEEE) is a Professor of Nanoelectronics at the University of Glasgow, where he leads the Electronics and Nanoscale Engineering Division and holds an EPSRC Open Fellowship. He directs the Microelectronics Lab (meLAB), focusing on micro/nanoelectronics for medical technologies and quantum computing. He is CTO and co-founder of Neuranics, a deep neurotech company developing magnetic sensors for wearable neural interfaces. Prof. Heidari is a Royal Society of Edinburgh Saltire Fellow and has held leadership roles in IEEE, including on the Sensors Council and Circuits and Systems Society Board of Governors. He is Associate Editor-in-Chief of IEEE Transactions on Biomedical Circuits and Systems and has chaired several major IEEE conferences. He has published over 280 peer-reviewed papers and received multiple awards, including the IET JA Lodge Award and IEEE Sensors Council Young Professional Award.